

PIV-Based 3D Fluid Flow Reconstruction Using Light Field Camera

Zhong Li¹, Jinwei Ye², Yu Ji⁴, Hao Sheng⁵ and Jingyi Yu^{1,3}

¹University of Delaware, Newark, DE, USA. lizhong@udel.edu

²Louisiana State University, Baton Rouge, LA, USA jye@csc.lsu.edu

³ShanghaiTech University, Shanghai, China. yujingyi@shanghaitech.edu.cn

⁴DGene, Inc. yu.ji@dgene.com

⁵Beihang University. shenghao@buaa.edu.cn

Abstract

Particle Imaging Velocimetry (PIV) estimates the flow of fluid by analyzing the motion of injected particles. The problem is challenging as the particles lie at different depths but have similar appearance and tracking a large number of particles is particularly difficult. In this paper, we present a PIV solution that uses densely sampled light field to reconstruct and track 3D particles. We exploit the refocusing capability and focal symmetry constraint of the light field for reliable particle depth estimation. We further propose a new motion-constrained optical flow estimation scheme by enforcing local motion rigidity and the Navier-Stoke constraint. Comprehensive experiments on synthetic and real experiments show that using a single light field camera, our technique can recover dense and accurate 3D fluid flows in small to medium volumes.

1. Introduction

Recovering time-dependent volumetric 3D fluid flow is a challenging but rewarding task with numerous applications in a broad range of science and engineering fields, including oceanology, geophysics, biology, mechanical and environmental engineering. Since most flows are transparent, capturing real 3D flows requires inserting tracking targets. In experimental fluid dynamic, the widely adopted methodology for visualizing and measuring the fluid flow is the Particle Imaging Velocimetry (PIV) [1]: by seeding the fluid with tracer particles that are assumed to faithfully follow the flow dynamics, the fluid flow (*i.e.*, the velocity field) is estimated from the particles' 3D motion trajectory.

Standard approaches such as laser scanning-based PIV [16, 6] use ultra high scanning-rate laser beam to illuminate particles and track their movement. However, since the

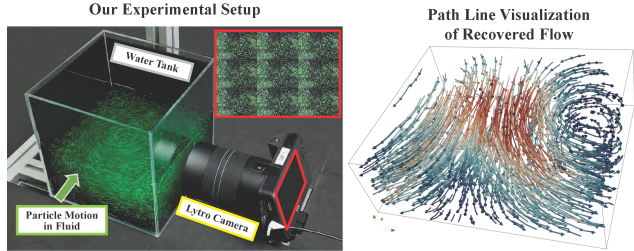


Figure 1. We use a commercial light field camera in PIV setting (left) to recover volumetric 3D fluid flow (right).

laser beam scans one depth layer at a time, the measured velocity field only contains 2D in-plane motion and is restricted on the scanned 2D fluid slice. To fully characterize the fluid, it is necessary to recover the flow motion in 3D for the entire fluid volume. Three-dimensional PIV such as tomographic PIV (Tomo-PIV) [9] use multiple cameras to capture the particles and resolve their 3D depth via multi-view stereo. These systems are bulky and expensive and each measurement requires elaborate calibration and synchronization. Most recently, the Rainbow PIV [45, 44] proposes to use color to encode the particle depth in order to recover the fluid flow in 3D. However, this setup requires specialized illumination source with diffractive optics for color-encoding and the optical system needs to be precisely aligned.

In this paper, we propose a flexible and low-cost 3D PIV solution that uses a lenslet-based light field camera as the acquisition device (See Fig. 1). A light field camera, in essence, is a single-shot, multi-view acquisition device [32]. The captured light field records 4D spatial and angular light rays scattered from the tracer particles. As commercial light field cameras can now capture high resolution light field (*e.g.*, Lytro Illum captures 40 megarays), we are able to acquire a dense set of particles in 3D fluid volume. The small

baseline of lenslet array helps to resolve subtle particle motions in sub-pixel level. In particular, our method benefits from the post-capture refocusing capability of light field and establish particle correspondences at different depth layers from the light field focal stack. To resolve heavily occluded particles, we exploit the focal stack symmetry (*i.e.*, intensities are symmetric in the focal stack around the ground truth disparity [25, 38]) for accurate particle 3D reconstruction.

Once we recover the 3D particle locations at individual frames, we present a novel physical-based optimization framework to recover dense volumetric 3D fluid flow (*i.e.*, 3D velocity field). Specifically, we introduce two new regularization terms to refine the variational optical flow [17]: 1) a one-to-one particle correspondence term to maintain smooth and consistent flow motions across different time frames; and 2) a divergence-free regularization term derived from the Navier-Stoke Equations to capture the physical properties of incompressible fluid. These terms help to resolve ambiguity caused by similar appearance of the particles while enforcing the reconstruction to obey physical laws. Through synthetic and real experiments, we show that our approach outperforms state-of-the-art PIV solutions on recovering volumetric 3D fluid flows of various types in small to medium fluid volumes.

2. Related Work

In computer vision and graphics, much effort has been made in modeling and recovering transparent objects or phenomena (*e.g.*, fluid [31, 47], gas flows [20, 19, 4, 27, 46], smoke [12, 14], and flames [13, 19], *etc.*) directly from images. As these objects do not have their own appearances, often a known pattern is assumed and light paths through the transparent medium are estimated for 3D reconstruction. A comprehensive survey can be found in [18]. However, many of these imaging techniques are designed to recover the 3D density field, which does not explicitly exhibit the internal flow motion.

Our approach is developed upon the Particle Imaging Velocimetry (PIV) method that estimates flow motion from movement of injected tracer particles. Traditional PIV [16, 6] recovers 2D velocity fields on thin fluid slices using high-speed laser scanning. As 3D volumetric flow is critical to fully characterize the fluid behavior, recovering 3D velocity fields within the whole volume is of great interest.

To resolve 3D particle fields, stereoscopic cameras [3, 34] are used to estimate the particle depth. Tomographic PIV (Tomo-PIV) [9, 35, 22] use multiple (usually three to six) cameras to determine 3D particle locations by space carving. Aguirre-Pablo *et al.* [2] perform Tomo-PIV using mobile devices. However, reconstruction accuracy is compromised. Other notable 3D PIV approaches include defocusing PIV [43, 21], Holographic PIV [48, 36], synthetic aperture PIV [5, 30] and light field PIV [41, 40]. All

these systems use an array of cameras for acquisition and each measurement requires elaborate calibration and synchronization. In contrast, our setup uses a single light field camera. A light field camera usually has smaller baseline and higher angular resolution than camera array and thus is more suitable to resolve small particles. Recently proposed rainbow PIV [45, 44] use color-coded illumination to recover depth from a single camera. However, both the light source and camera are customized with special optical elements and only sparse set of particles can be resolved. Proof-of-concept simulations [26] and experiments [10] using compact light field or plenoptic cameras for PIV have been performed and showed efficacy. However, the depth estimation and particle tracking algorithms used in these methods are not optimized for light fields. In our approach, focal stack symmetry [25] of densely sampled light field is exploited for more accurate depth reconstruction in presence of heavily occluded dense particles.

To recover the flow motion, standard PIV uses 3D cross-correlation to match local windows between neighboring time frames [9, 42]. Although many improvements (for instance, matching with adaptive window sizes [22]) have been made, the window-based solutions suffer problems at regions with few visible particles. Another class of methods directly track the path of individual particles over time [28, 35]. However, with increased particle density, tracking is challenging under occlusions. Heitz *et al.* [15] advocate the application of variational optical flow to fluid flow estimation. A recent trend [45, 23] is to incorporate physical constraints such as Stokes equation into optical flow framework to recover flows that obey physical laws. However, many physical-based regularizations are in high-orders that are complex to solve. In our approach, we introduce two novel regularization terms: 1) particle correspondence term and 2) divergence free term to refine the basic variational optical flow framework [17] for improved accuracy and efficiency.

3. Our Approach

Fig. 2 shows our algorithmic pipeline of volumetric 3D fluid flow reconstruction using light field PIV. For each time frame, we first detect particles in light field sub-aperture images using the IDL particle detector [7]. We then estimate particle depths through a joint optimization that exploits light field properties. After we obtain 3D particle locations, we compare two consecutive frames to establish one-to-one particle correspondences and finally solve the 3D velocity field using a constrained optical flow.

3.1. 3D Particle Reconstruction

We first describe our 3D particle reconstruction algorithm that exploits properties of light field.

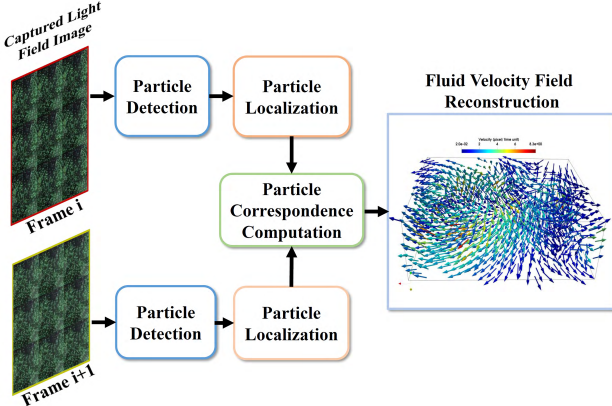


Figure 2. Our algorithmic pipeline for reconstructing volumetric 3D fluid flow from particle light fields.

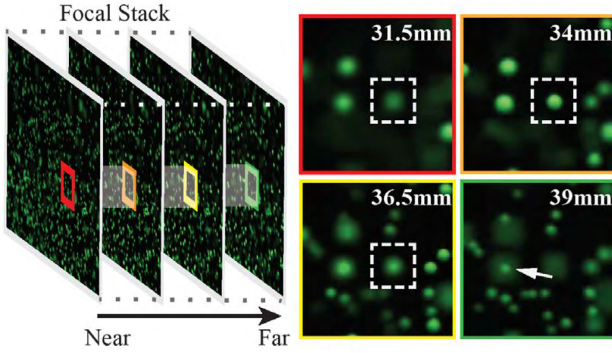


Figure 3. Focal stack symmetry. We show zoom-in views of four focal slices on the right. A particle exhibits symmetric defocus effect (e.g., 31.5mm and 36.5mm slices) centered at the in-focus slice (34mm). In the 39mm slice, an occluded particle could be seen as the occluder becomes extremely out-of-focus.

Focal Stack Symmetry. A focal stack is a sequence of images focused at different depth layers. Due to the post-capture refocusing capability, a focal stack can be synthesized from a light field by integrating recorded rays. Lin *et al.* [25] conduct symmetry analysis on focal stacks and show that *non-occluding* pixels in a focal stack exhibit symmetry along the focal dimension centered at the in-focus slice. In contrast, occluding boundary pixels exhibit local asymmetry as the outgoing rays are not originated from the same surface. Such property is called focal stack symmetry. As shown in Fig. 3, in a focal stack, a particle exhibits symmetric defocus effect centered at the in-focus slice. It's also worth noting that occluded particles could be seen in the focal stack as the occluder becomes extremely out-of-focus. Utilizing the focal stack symmetry helps resolve heavily occluded particles and hence enhances the accuracy and robustness of particle depth estimation.

Given a particle light field, we synthesize a focal stack from sub-aperture images by integrating rays from the same

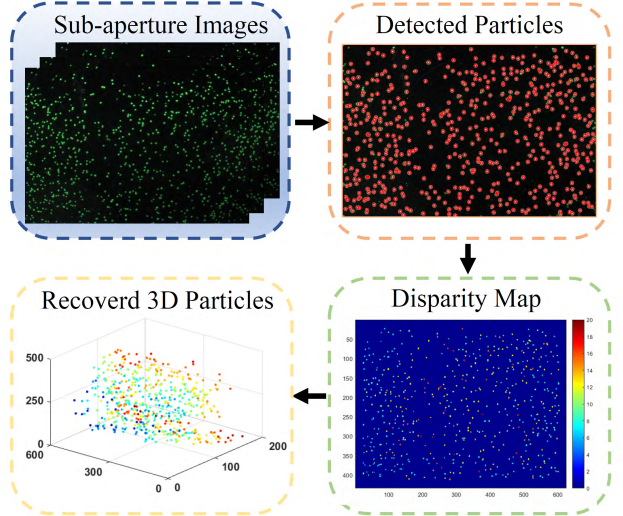


Figure 4. Our 3D particle reconstruction workflow.

focal slice. Each focus slice f has a corresponding disparity d that indicates the in-focus depth layer. Let $I(p, f)$ be the intensity of a pixel p at focal slice f . For symmetry analysis, we define an in-focus score $\kappa(p, f)$ a pixel p at focal slice f as:

$$\kappa(p, f) = \int_0^{\delta_{max}} \rho(I(p, f + \delta) - I(p, f - \delta)) d\delta \quad (1)$$

where δ represents tiny disparity/focal shift and δ_{max} is maximum shift amount; $\rho(\nu) = 1 - e^{-|\nu|_2/(2\sigma^2)}$ is a robust distance function with σ controlling its sensitivity to noises. According to the focal stack symmetry, the intensity profile $I(p, f)$ is locally symmetric around the true surface depth. Therefore, if the pixel p is in focus at its true depth sparsity \hat{d} , $\kappa(p, \hat{d})$ should be 0. Hence given an estimated disparity d at p , the closer distance between d and \hat{d} , the smaller the $\kappa(p, d)$. We then formulate the focal stack symmetry term for depth optimization by summing up $\kappa(p, d)$ for all pixels in a focal slice f with disparity d :

$$\beta_{fs}(d) = \sum_p \kappa(p, d) \quad (2)$$

Color and Gradient Consistency. Besides the focal stack symmetry, we also consider the color and gradient data consistency across sub-aperture images for depth estimation using data terms similar to [25]. Specifically, by comparing each sub-aperture image with the center view, we define a cost metric $C(i, p, d)$ as:

$$C(i, p, d) = |I_c(\omega(p)) - I_i(\omega(p + d(p)\chi(i)))| \quad (3)$$

where i is the sub-aperture image index; I_c and I_i refers to the center view and sub-aperture image respectively; $\omega(p)$

refers to a small local window centered around pixel p ; $d(p)$ is an estimate disparity at pixel p ; and $\chi(i)$ is a scalar that scale the disparity $d(p)$ according to the relative position between I_c and I_i as $d(p)$ is the pixel-shift between neighboring sub-aperture images.

The cost metric C measures the intensity similarity between shifted pixels in sub-aperture images given an estimated disparity. By summing up C for all pixels, we obtain the sum of absolute differences (SAD) term for color consistency measurement:

$$\beta_{sad}(d) = \frac{1}{N} \sum_{i \in N} \sum_p C \quad (4)$$

where N is the total number of sub-aperture images (excluding the center view).

Besides the color consistency, we also consider the consistency in gradient domain. We first take partial derivatives of cost metric C (Eq. 3) in both x and y directions: $D_x = \partial C / \partial x$ and $D_y = \partial C / \partial y$ and then formulate the following weighted sum of gradient differences (GRAD) for gradient consistency measurement:

$$\beta_{grad}(d) = \frac{1}{N} \sum_{i \in N} \sum_p \mathcal{W}(i) \mathcal{D}_x + (1 - \mathcal{W}(i)) \mathcal{D}_y \quad (5)$$

In Eq. 5, $\mathcal{W}(i)$ is a weighing factor that determines the contribution of horizontal gradient cost (\mathcal{D}_x) according to the relative positions of the two sub-aperture images being compared. It is defined as $\mathcal{W}(i) = \frac{\Delta i_x}{\Delta i_x + \Delta i_y}$, where Δi_x and Δi_y are the position differences between sub-aperture images along x and y directions. For example, $\mathcal{W}(i) = 1$ if the target view is located at the horizontal extent of the reference view. In this case, only the gradient costs in the x direction are aggregated.

Particle Depth Estimation. Finally, combining Eq. 2, 4, and 5, we can form the following energy function for particle depth (disparity) estimation:

$$\beta(d) = \beta_{fs}(d) + \lambda_{sad}\beta_{sad}(d) + \lambda_{grad}\beta_{grad}(d) \quad (6)$$

Eq. 6 can be optimized using the Levenberg-Marquardt (LM) algorithm. In our experiments, the two weighting factors are picked as $\lambda_{sad} = 0.8$ and $\lambda_{grad} = 0.9$.

Finally, using the calibrated light field camera intrinsic parameters, we are able to convert the particle disparity map to 3D particle location. Our 3D particle reconstruction scheme with intermediate results is shown in Fig. 4.

3.2. Fluid Flow Reconstruction

After we reconstruct 3D particles in each frame, we compare two consecutive frames to estimate the volumetric 3D fluid flow.

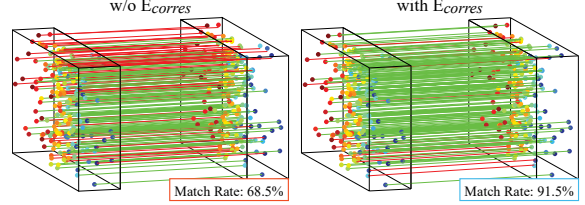


Figure 5. Particle matching between source and target volumes with vs. without using the correspondence term E_{corres} . In our plots, green lines indicate correct correspondences and red lines indicate incorrect ones.

Given two sets of particle locations S_1 and S_2 recovered from consecutive frames, we first convert S_1 and S_2 into voxelized 3D volumes as occupancy probabilities Θ_1 and Θ_2 through linear interpolation. Our goal is to solve per-voxel 3D velocity vector $\mathbf{u} = [u, v, w]$ for the whole volume.

In particular, we solve this problem under the variational optical flow framework [17] and develop two novel regularization terms, correspondence term and divergence-free term, for improved accuracy and efficiency. Therefore, our overall energy function E_{total} is combination of regularization terms and can be written as follow:

$$E_{total} = E_{data} + \lambda_1 E_{smooth} + \lambda_2 E_{corres} + \lambda_3 E_{div} \quad (7)$$

where λ_1 , λ_2 , and λ_3 are term balancing factors. In the following, we describe the algorithmic details of each regularization term.

Basic Optical Flow. The data term E_{data} and smooth term E_{smooth} are adopted from basic optical flow that derived from the brightness constancy assumption. E_{data} enforces consistency between occupancy possibilities Θ_1 and Θ_2 at corresponding voxels and E_{smooth} constrain the fluid motion to be piece-wise smooth. In our case, E_{data} and E_{smooth} can be written as:

$$E_{data}(\mathbf{u}) = \int ||\Theta_2(\mathbf{p} + \mathbf{u}) - \Theta_1(\mathbf{p})||_2^2 d\mathbf{p} \quad (8)$$

$$E_{smooth}(\mathbf{u}) = ||\nabla \cdot \mathbf{u}||_2^2 \quad (9)$$

where \mathbf{p} refers to a voxel in fluid volume and ∇ is the gradient operator.

Correspondence Term. We propose a novel correspondence term for more accurate flow estimation. Notice that E_{data} in the basic optical flow only enforces voxel-level consistency while particle-to-particle correspondences

are not guaranteed. We therefore develop a correspondence term E_{corres} to enforce one-to-one particle matching. E_{corres} helps improve matching accuracy especially in regions with lower particle density.

Let's consider two sets of particles: $S_1 = \{s_1 | s_1 \in \mathbb{R}^3\}$ as reference and $S_2 = \{s_2 | s_2 \in \mathbb{R}^3\}$ as target. E_{corres} enforces the one-to-one particle matching between the target and reference sets. To formulate E_{corres} , we first estimate correspondences between particles in S_1 and S_2 . We solve this problem by estimating transformations that map particles in S_1 to S_2 .

In particular, we employ a deformable graph similar to [39] that considers local geometric similarity and rigidity. To build the graph, we uniformly sample a set of particles in S_1 and use them as graph nodes $\mathbf{G} = \{g_1, g_2, g_3, \dots, g_m\}$. We then aim to estimate a set of affine transformations $\mathbf{A} = \{A_i\}_{i=1}^m$ and $\mathbf{b} = \{b_i\}_{i=1}^m$ for each graph node. We then use these graph nodes as control points to deform particles in S_1 instead of computing transformations for individual particles. Given the graph node transformations \mathbf{A} and \mathbf{b} , we can transform every particle $s_1 \in S_1$ to its new location s'_1 using a weighted linear combination of graph nodes transformations:

$$s'_1 = f(s_1, \mathbf{A}, \mathbf{b}) = \sum_{i=1}^m \varpi_i(s_1)(\mathbf{A}(s_1 - g_i) + g_i + b_i) \quad (10)$$

where the weight $\varpi_i(s_1) = \max(0, (1 - \|s_1 - g_i\|^2/R^2)^3)$ models a graph node g_i influence on a particle $s_1 \in S_1$ according to their Euclidean distance. This restricts the particle transformation to be only affected by nearby graph nodes. In our experiment, we consider the nearest four graph nodes and R is the particle's distance to its nearest graph node.

To obtain the graph node transformations \mathbf{A} and \mathbf{b} , we solve an optimization problem with energy function:

$$\Psi_{total} = \Psi_{data} + \alpha_1 \Psi_{rigid} + \alpha_2 \Psi_{smooth} \quad (11)$$

Ψ_{data} is the data term aims to minimize particle-to-particle distances after transformation and is thus formulated as:

$$\Psi_{data} = \sum_{s_1 \in S_1} \|s'_1 - c_i\|^2 \quad (12)$$

where c_i is the closest point to s'_1 in S_2 .

Ψ_{rigid} is a rigidity regularization term that enforces the local rigidity of affine transformation. Ψ_{rigid} can be written as:

$$\Psi_{rigid} = \sum_{\mathbf{G}} \|A_i^T A_i - \mathbb{I}\|_F^2 + (\det(A_i) - 1)^2 \quad (13)$$

where \mathbb{I} is an identity matrix.

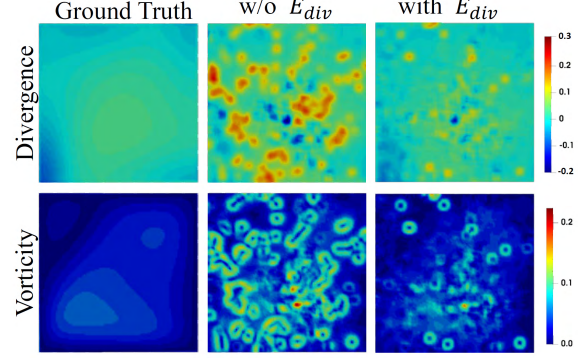


Figure 6. Recovered fluid slice divergence and vorticity magnitudes with vs. without using the divergence-free term E_{div} .

The last term Ψ_{smooth} enforces the spatial smoothness of nearby nodes and is written as:

$$\Psi_{smooth} = \sum_{\mathbf{G}} \sum_{k \in \Omega(i)} \|A_i(g_k - g_i) + g_i + b_i - (g_k + b_k)\|^2 \quad (14)$$

where $\Omega(i)$ refers to the set of nearest four neighbors of g_i .

The overall energy function Ψ_{total} can be optimized with an iterative Gauss-Newton algorithm and the affine transformations \mathbf{A} and \mathbf{b} are thus solved. In our experiment, we use $\alpha_1 = 50$ and $\alpha_2 = 10$ for Eq. 11.

By applying Eq. 11, we can transform every particle $s_1 \in S_1$ to its new location s'_1 using the graph nodes' transformations. We then find S_1 's corresponding set S_2^c in the target S_2 using a nearest neighbor search (*i.e.*, $s_2^c = \text{nnsearch}(s'_1, s_2)$). After we establish the one-to-one correspondences between S_1 and S_2 , our correspondence term can be formulated based on the color consistency assumption as follow:

$$E_{corres}(\mathbf{u}, S_1, S_2^c) = \sum_{s_1 \in S_1, s_2^c \in S_2^c} \|s_2^c - (s_1 + \mathbf{u}(s_1))\|_2^2 \quad (15)$$

We show the effectiveness of the correspondence term by comparing the velocity field obtained with vs. without E_{corres} . The results are shown in Fig. 5. This comparison demonstrates that our correspondence term greatly improves matching accuracy and hence benefits flow reconstruction.

Divergence-Free Term. To capture the physical properties of incompressible fluid, we add a divergence-free regularization term E_{div} to the optical flow framework. Based on the Navier-Stoke functions, fluid velocity \mathbf{u} can be split into two distinct components: irrotational component ∇P and solenoidal component $\mathbf{u}_{sol} = [u_{sol}, v_{sol}, w_{sol}]$ with the Helmholtz decomposition. The Irrotational component ∇P is curl-free and is determined by the gradient of

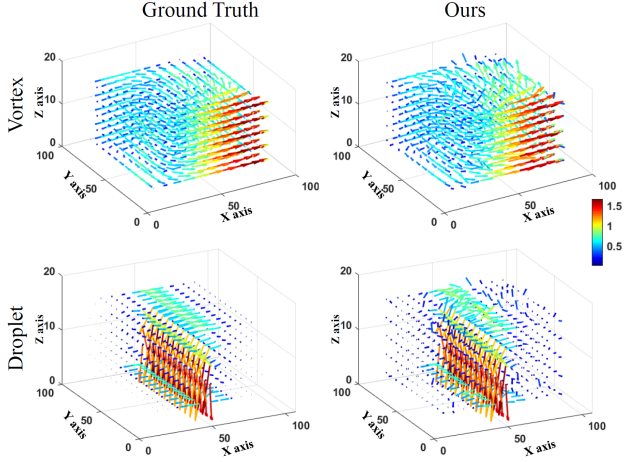


Figure 7. We compare our recovered flow velocity field (right) with the ground truth (left) on two simulated flows: vortex (top) and droplet (bottom).

a scalar function P (e.g., pressure). The solenoidal component \mathbf{u}_{sol} is divergence-free and models an incompressible flow. From the divergence-free property, we have:

$$\nabla \cdot \mathbf{u}_{sol} = 0 \quad (16)$$

where $\nabla = [\frac{\partial}{\partial x}, \frac{\partial}{\partial y}, \frac{\partial}{\partial z}]^T$ is the divergence operator. Since $\mathbf{u} = \mathbf{u}_{sol} + \nabla P$, taking divergence on both sides, we have:

$$\nabla \cdot \mathbf{u} = \nabla^2 P \quad (17)$$

We solve Eq. 17 by Poisson integration and compute the scalar field as $P = (\nabla^2)^{-1}(\nabla \cdot \mathbf{u})$. We then project \mathbf{u} into the divergence-free vector field: $\mathbf{u}_{sol} = \mathbf{u} - \nabla P$. Similar to [11], we formulate a divergence-free term E_{div} that enforces the flow velocity field \mathbf{u} close to its divergence-free component \mathbf{u}_{sol} :

$$E_{div}(\mathbf{u}) = \|\mathbf{u} - \mathbf{u}_{sol}\|_2^2 \quad (18)$$

We perform fluid flow experiment with vs. without E_{div} . Results shown in Fig. 6 are the divergence and vorticity magnitudes of the center fluid slice. We can see that with E_{div} , both divergence and vorticity are closer to the ground truths.

Optimization. Finally we optimize the energy function E_{total} (Eq. 7) to recover the volumetric 3D velocity field. As all the terms are in L2-norm, we can take the derivative of \mathbf{u} to reduce the problem to a linear system. Specifically, given an initial velocity field, Next we would like to minimized E_{total} in order to reconstruct fluid flow velocity field. We solve this optimization problem via variational framework. Our solver first assumes that a current estimate of the flow field is \mathbf{u} , and now

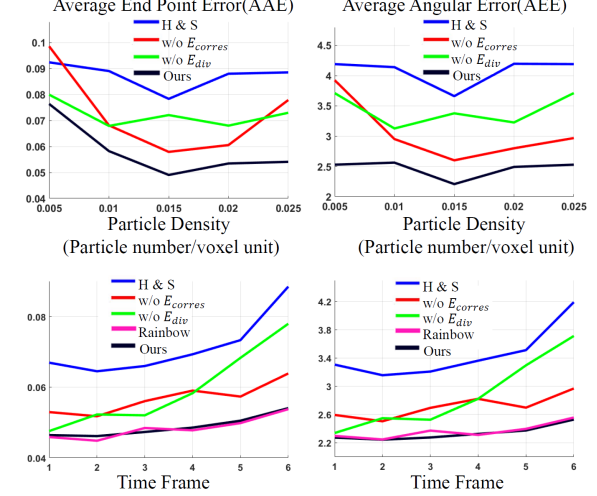


Figure 8. Quantitative evaluation of various methods on the vortex scene. upper-left and upper-right show errors with respect to different particle densities. lower-left and lower-right show accumulated errors over time.

we need to estimate the increment $\Delta \mathbf{u}$ in every iteration. Therefore, the objective function $E_{total}(\mathbf{u})$ is changed to $E_{total}(\Delta \mathbf{u})$. The main method to solve $E_{total}(\Delta \mathbf{u})$ is to find $\Delta \mathbf{u} = [\Delta u, \Delta v, \Delta w]$, such that gradient on $\frac{\partial E_{total}}{\partial u}, \frac{\partial E_{total}}{\partial v}, \frac{\partial E_{total}}{\partial w}$ is equal to 0. For ease of computation, we vectorize $u, v, w, u_{sol}, v_{sol}, w_{sol}, \Delta u, \Delta v, \Delta w$ into column vectors $U, V, W, U_{sol}, V_{sol}, W_{sol}, \Delta U, \Delta V, \Delta W$. $\Theta_{x,y,z}$ is the partial derivative of $\Theta_2(p + \mathbf{u})$ at x,y,z direction respectively, and $\Theta_t = \Theta_2(p + \mathbf{u}) - \Theta_1$. Let the $\Theta_x = diag(\Theta_x)$, $\Theta_y = diag(\Theta_y)$, $\Theta_z = diag(\Theta_z)$ and $\Theta_t = diag(\Theta_t)$ be diagonal matrices where the diagonal values are vectorized volumes of $\Theta_x, \Theta_y, \Theta_z, \Theta_t$. Then we solve the energy function by solving a linear system $\mathcal{A}\mathbf{x} = \tilde{b}$. \mathbf{x} is $\Delta \mathbf{u}^T$.

$$\mathcal{A} = \begin{bmatrix} \Theta_x^2 + \mathcal{F} & \Theta_x \Theta_y & \Theta_x \Theta_z \\ \Theta_x \Theta_y & \Theta_y^2 + \mathcal{F} & \Theta_y \Theta_z \\ \Theta_x \Theta_z & \Theta_y \Theta_z & \Theta_z^2 + \mathcal{F} \end{bmatrix} \quad (19)$$

$$\tilde{b} = \begin{bmatrix} -(\Theta_x \Theta_t + \mathcal{F}U - \lambda_2 FU_c - \lambda_3 F_{\perp}U_{sol}) \\ -(\Theta_y \Theta_t + \mathcal{F}V - \lambda_2 FW_c - \lambda_3 F_{\perp}V_{sol}) \\ -(\Theta_z \Theta_t + \mathcal{F}W - \lambda_2 FW_c - \lambda_3 F_{\perp}W_{sol}) \end{bmatrix} \quad (20)$$

Where Laplacian filter is defined as $L = D_x^T D_x + D_y^T D_y + D_z^T D_z$, D_x, D_y, D_z corresponding to x, y, z direction filters respectively. $\mathcal{F} = \lambda_1 L + \lambda_2 F + \lambda_3 F_{\perp}$. F_{\perp} is an identity matrix. U_c, V_c and W_c correspond to sparse displacement computed by sparse correspondence in Section 3.2, and masked out by F . Please refer to the supplemental material for more details on derivation of the linear system.

Furthermore, in order to improve accuracy, we perform the optimization under a multi-layer coarse-to-fine scheme

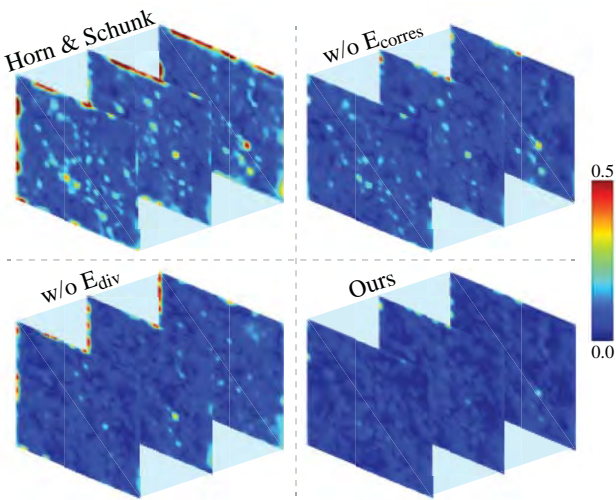


Figure 9. Error maps of velocity field in three slices within the vortex fluid volume.

using Gaussian pyramids. Typically, the initial value of \mathbf{u} is set to zero. We update the value of each level by propagating $\Delta\mathbf{u}$ from coarser scale levels.

4. Experimental Results

To evaluate our approach, we conduct experiments on both synthetic and real fluid flows. We also test on the John Hopkins Turbulence Database (JHUTDB) [24, 33] that provides ground truth flows. All computations are performed on a PC with Intel i7-4700K CPU and 16G memory. On average, our entire process takes around 2 minutes, which includes 30 seconds on particle location estimation, 40 seconds on correspondence matching, and 50 seconds on velocity field reconstruction.

4.1. Synthetic Results

We first evaluate our proposed approach on simulated fluid flow. We simulate two types of flows: a vortex flow and a drop flow within a volume of $100 \times 100 \times 20$. We randomly sample tracer particles within the fluid volume. As result, the particle density is 0.02 per voxel. We render light fields images with angular resolution 7×7 and spatial resolution 434×625 . We simulate the advection of particles over time following the method in [37].

We apply our algorithms on the rendered light fields to recover 3D fluid flows. In Fig. 7, we visualize the velocity field as vector field and compare our reconstructions with the ground truth ones. Qualitatively, our reconstructed vector fields are highly consistent with the ground truths. We also perform quantitative evaluations using two error metrics: the average end-point error (AEE) and the average angular error (AAE). We compare our method with the multi-scale Horn-Schunck (H&S) [29] and the rainbow PIV [45].

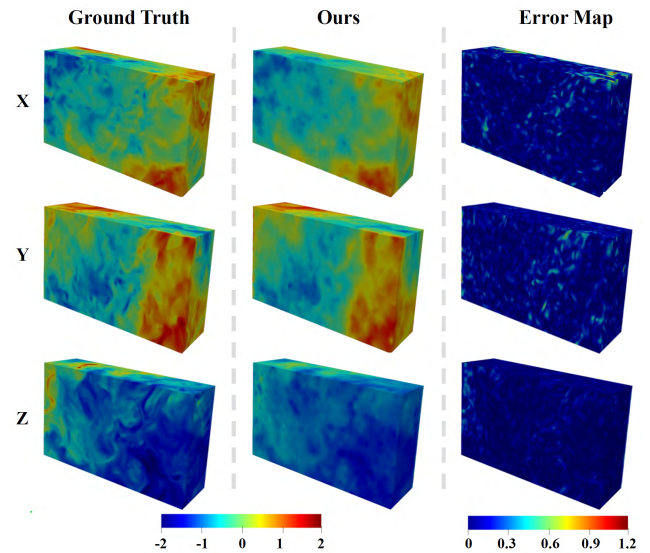


Figure 10. JHUTDB velocity field reconstruction results. We illustrate the magnitudes of the velocity field along x, y, and z directions with color-coding.

Specifically, we apply H&S on our recovered 3D particles and use it as baseline algorithm for flow estimation. With this comparison, we hope to demonstrate the effectiveness of our regularization terms in flow estimation. For rainbow PIV, we have implemented a renderer to generate depth-dependent spectral images of virtual particles. To ensure fairness, the rendered images have the same spatial resolution as our input light field (*i.e.*, 434×625).

We evaluate our method, our method without correspondence term (w/o E_{corres}), our method without divergence term (w/o E_{div}), H&S, and rainbow PIV with respect to particle density and time accumulation. The resulting AEE and AAE are plotted in Fig. 8. For varying particle density, our method (including its variations without E_{corres} or E_{div}) outperforms H&S in most cases. Our method without the correspondence term is slightly worse than H&S method on AEE when the particle density is 0.005. This is because when the particle density is too low, the divergence term over-smoothes the velocity field. We can see that our method is quite robust with the change of particle density. In order to further illustrate the effectiveness of our regularization terms (E_{corres} and E_{div}), we visualize the error maps of velocity field obtained with different methods on several fluid volume slices (see Fig. 9). This experiment is performed on the vortex flow with particle density 0.02. We can see that the best performance is achieved when both regularization terms are imposed. The errors are expected to accumulate when processing a sequence of fluid flow. Fig. 8 (c) and (d) show that our error accumulation rate is much slower than H&S and is comparable with rainbow PIV which considers temporal consistency.

	H&S	Ours w/o E_{corres}	Ours w/o E_{div}	Ours
AAE	4.9950	4.8696	4.5304	4.4625
AEE	0.1669	0.1621	0.1511	0.1483

Table 1. Quantitative evaluation of various methods on JHUTDB.

4.2. JHUTDB Results

We then test our method on the the Johns Hopkins Turbulence Database (JHUTDB) [24]. To reduce processing time, we crop out a volume of $256 \times 128 \times 80$ voxels for each turbulence in the dataset. We generate random tracer particles with density 0.025 per voxels and advect the particles according to the turbulence velocity field. Similar to our synthetic experiments, we render light field images of the tracer particles and apply our algorithms to estimate 3D particle locations and 3D flow velocity field. We show our reconstruction in comparison with the ground truth velocity field in Fig. 10. Specifically, we use color-coded volumes to illustrate the magnitudes of the velocity field along x, y, and z directions. The error map indicates our method is highly accurate in most voxels. For quantitative evaluation, we also compute the AAE and AEE of our method in comparison with H&S and variations of our method. The results are shown in Table 1.

4.3. Real Results

Experiment Setup. Our PIV-based fluid flow acquisition system is shown in Fig. 1. We use a Lytro Illum light field camera with 30mm focal length to capture the tracer particles in fluid. As Illum does not have video mode, we use an external control board to trigger the camera at high frequency to capture consecutive time frames. Due to the limitation of on-chip image buffer size, our acquisition cannot achieve very high frame rate. In our experiment, we set the trigger frequency to be 10 Hz (*i.e.*, we capture 10 images per second). The capture light field has angular resolution 15×15 and spatial resolution 625×434 . We use the light field calibration toolbox [8] to process and decode raw light field data into sub-aperture images. We further remove undesired refraction distortions using checkerboard images captured at various depth in the fluid volume. We use the center view as reference for depth estimation and the effective depth volume that we are able to reconstruct is around $600 \times 500 \times 200$ (mm).

We use green polyethylene microspheres with density 1g/cc and size 1000-1180 μm as tracer particles. Before dispersing the particles, we mix some surfactant with the particles to reduce surface tension caused by water in order to minimize agglomeration between particles. We test on three types of flows: vortex, double vortex, and random complex flows. Fig. 11 shows our recovered fluid flow velocity field and path line visualization (please refer to the supplemental material for more reconstruction results).

The velocity field is computed between the first and second frame. The path line visualization is computed using four consecutive frames. We can see that our reconstructions well depicts the intended fluid motions and are thus reliable.

5. Conclusion

In this paper, we have presented a novel PIV solution that uses a commercial compact light field camera to recover volumetric 3D fluid motion. We have developed a 3D particle reconstruction algorithm by exploiting the light field focal stack symmetry in order to handle heavily occluded particles. To recover the fluid flow, we have refined the classical optical flow framework by introducing two novel regularization terms: 1) a correspondence term to enforce one-to-one particle matching; and 2) a divergence-free term to capture the physical properties of incompressible fluid. Comprehensive synthetic and real experiments have demonstrated the effectiveness of our method.

References

- [1] R. J. Adrian and J. Westerweel. *Particle image velocimetry*. Number 30. Cambridge University Press, 2011. 1
- [2] A. A. Aguirre-Pablo, M. K. Alarfaj, E. Q. Li, J. F. Hernández-Sánchez, and S. T. Thoroddsen. Tomographic particle image velocimetry using smartphones and colored shadows. In *Scientific Reports*, 2017. 2
- [3] M. Arroyo and C. Greated. Stereoscopic particle image velocimetry. *Measurement science and technology*, 2(12):1181, 1991. 2
- [4] B. Atcheson, I. Ihrke, W. Heidrich, A. Tevs, D. Bradley, M. Magnor, and H.-P. Seidel. Time-resolved 3d capture of non-stationary gas flows. In *ACM transactions on graphics (TOG)*, volume 27, page 132. ACM, 2008. 2
- [5] J. Belden, T. T. Truscott, M. C. Axiak, and A. H. Techet. Three-dimensional synthetic aperture particle image velocimetry. *Measurement Science and Technology*, 21(12):125403, 2010. 2
- [6] C. Brücker. 3d scanning piv applied to an air flow in a motored engine using digital high-speed video. *Measurement Science and Technology*, 8(12):1480, 1997. 1, 2
- [7] J. C. Crocker and D. G. Grier. Methods of digital video microscopy for colloidal studies. *Journal of colloid and interface science*, 179(1):298–310, 1996. 2
- [8] D. G. Dansereau, O. Pizarro, and S. B. Williams. Decoding, calibration and rectification for lenslet-based plenoptic cameras. In *Proceedings of the IEEE conference on computer vision and pattern recognition*, pages 1027–1034, 2013. 8
- [9] G. E. Elsinga, F. Scarano, B. Wieneke, and B. W. van Oudheusden. Tomographic particle image velocimetry. *Experiments in fluids*, 41(6):933–947, 2006. 1, 2
- [10] T. Fahringer and B. Thurow. Tomographic reconstruction of a 3-d flow field using a plenoptic camera. In *42nd AIAA Fluid Dynamics Conference and Exhibit*, page 2826, 2012. 2

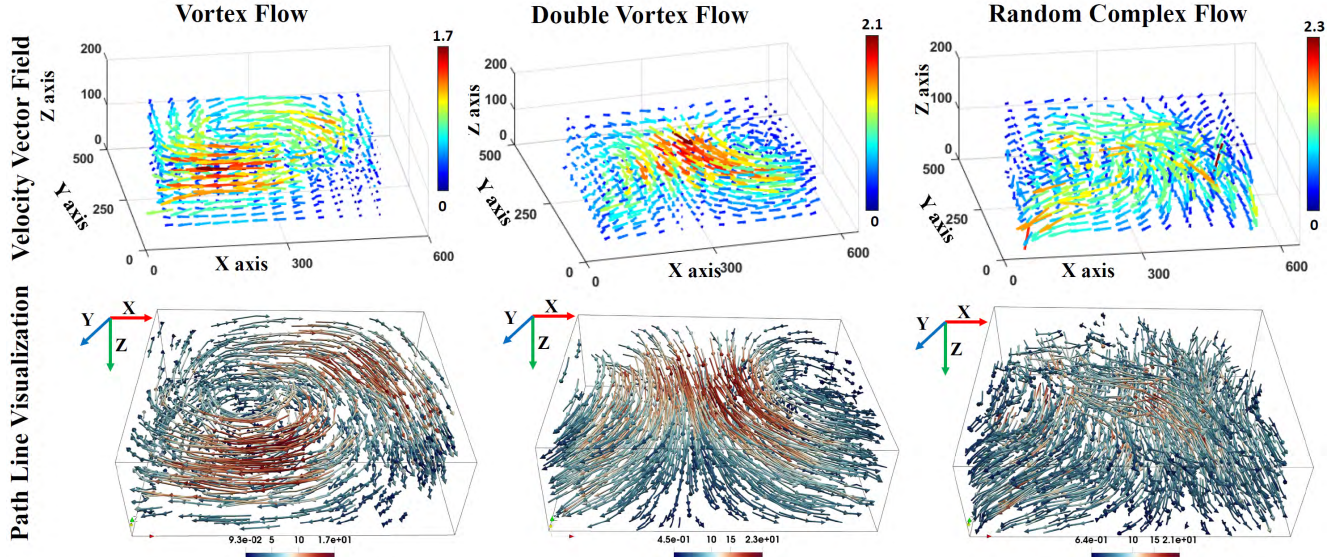


Figure 11. Real experiment results. We show our recovered velocity fields (left) and path line visualizations on four consecutive frames (right) for three types of flows: vortex, double vortex and a random complex flow.

- [11] J. Gregson, I. Ihrke, N. Thuerey, and W. Heidrich. From capture to simulation: connecting forward and inverse problems in fluids. *ACM Transactions on Graphics (TOG)*, 33(4):139, 2014. [6](#)
- [12] J. Gu, S. K. Nayar, E. Grinspun, P. N. Belhumeur, and R. Ramamoorthi. Compressive structured light for recovering inhomogeneous participating media. *IEEE Transactions on Pattern Analysis and Machine Intelligence*, 35:1–1, 2013. [2](#)
- [13] S. W. Hasinoff and K. N. Kutulakos. Photo-consistent reconstruction of semitransparent scenes by density-sheet decomposition. *IEEE Transactions on Pattern Analysis and Machine Intelligence*, 29:870–885, 2007. [2](#)
- [14] T. Hawkins, P. Einarsson, and P. Debevec. Acquisition of time-varying participating media. In *ACM Transactions on Graphics (ToG)*, volume 24, pages 812–815. ACM, 2005. [2](#)
- [15] D. Heitz, E. Mémin, and C. Schnörr. Variational fluid flow measurements from image sequences: synopsis and perspectives. *Experiments in fluids*, 48(3):369–393, 2010. [2](#)
- [16] T. Hori and J. Sakakibara. High-speed scanning stereoscopic piv for 3d vorticity measurement in liquids. *Measurement Science and Technology*, 15(6):1067, 2004. [1, 2](#)
- [17] B. K. Horn and B. G. Schunck. Determining optical flow. *Artificial intelligence*, 17(1-3):185–203, 1981. [2, 4](#)
- [18] I. Ihrke, K. N. Kutulakos, H. P. Lensch, M. Magnor, and W. Heidrich. Transparent and specular object reconstruction. In *Computer Graphics Forum*, volume 29, pages 2400–2426. Wiley Online Library, 2010. [2](#)
- [19] I. Ihrke and M. A. Magnor. Image-based tomographic reconstruction of flames. In *Symposium on Computer Animation*, 2004. [2](#)
- [20] Y. Ji, J. Ye, and J. Yu. Reconstructing gas flows using light-path approximation. *2013 IEEE Conference on Computer Vision and Pattern Recognition*, pages 2507–2514, 2013. [2](#)
- [21] L. Kajitani and D. Dabiri. A full three-dimensional characterization of defocusing digital particle image velocimetry. *Measurement Science and Technology*, 16(3):790, 2005. [2](#)
- [22] K. Lasinger, C. Vogel, and K. Schindler. Volumetric flow estimation for incompressible fluids using the stationary stokes equations. In *2017 IEEE International Conference on Computer Vision (ICCV)*, pages 2584–2592. IEEE, 2017. [2](#)
- [23] K. Lasinger, C. Vogel, and K. Schindler. Volumetric flow estimation for incompressible fluids using the stationary stokes equations. *2017 IEEE International Conference on Computer Vision (ICCV)*, pages 2584–2592, 2017. [2](#)
- [24] Y. Li, E. Perlman, M. Wan, Y. Yang, C. Meneveau, R. Burns, S. Chen, A. Szalay, and G. Eyink. A public turbulence database cluster and applications to study lagrangian evolution of velocity increments in turbulence. *Journal of Turbulence*, (9):N31, 2008. [7, 8](#)
- [25] H. Lin, C. Chen, S. Bing Kang, and J. Yu. Depth recovery from light field using focal stack symmetry. In *Proceedings of the IEEE International Conference on Computer Vision*, pages 3451–3459, 2015. [2, 3](#)
- [26] K. Lynch, T. Fahringer, and B. Thurow. Three-dimensional particle image velocimetry using a plenoptic camera. In *50th AIAA Aerospace Sciences Meeting including the New Horizons Forum and Aerospace Exposition*, page 1056, 2012. [2](#)
- [27] C. Ma, X. Lin, J. Suo, Q. Dai, and G. Wetzstein. Transparent object reconstruction via coded transport of intensity. In *Proceedings of the IEEE Conference on Computer Vision and Pattern Recognition*, pages 3238–3245, 2014. [2](#)
- [28] H. Maas, A. Gruen, and D. Papantoniou. Particle tracking velocimetry in three-dimensional flows. *Experiments in Fluids*, 15(2):133–146, 1993. [2](#)
- [29] E. Meinhardt, J. S. Pérez, and D. Kondermann. Horn-schunck optical flow with a multi-scale strategy. *IPOL Journal*, 3:151–172, 2013. [7](#)

- [30] L. Mendelson and A. H. Techet. Quantitative wake analysis of a freely swimming fish using 3d synthetic aperture piv. *Experiments in Fluids*, 56(7):135, 2015. [2](#)
- [31] N. J. Morris and K. N. Kutulakos. Dynamic refraction stereo. *IEEE transactions on pattern analysis and machine intelligence*, 33(8):1518–1531, 2011. [2](#)
- [32] R. Ng, M. Levoy, M. Brédif, G. Duval, M. Horowitz, P. Hanrahan, et al. Light field photography with a hand-held plenoptic camera. *Computer Science Technical Report CSTR*, 2(11):1–11, 2005. [1](#)
- [33] E. Perlman, R. Burns, Y. Li, and C. Meneveau. Data exploration of turbulence simulations using a database cluster. In *Proceedings of the 2007 ACM/IEEE conference on Supercomputing*, page 23. ACM, 2007. [7](#)
- [34] S. Pick and F.-O. Lehmann. Stereoscopic piv on multiple color-coded light sheets and its application to axial flow in flapping robotic insect wings. *Experiments in fluids*, 47(6):1009, 2009. [2](#)
- [35] D. Schanz, S. Gesemann, and A. Schröder. Shake-the-box: Lagrangian particle tracking at high particle image densities. *Experiments in fluids*, 57(5):70, 2016. [2](#)
- [36] J. Soria and C. Atkinson. Towards 3c-3d digital holographic fluid velocity vector field measurementtomographic digital holographic piv (tomo-hpiv). *Measurement science and technology*, 19(7):074002, 2008. [2](#)
- [37] J. Stam. Stable fluids. In *Proceedings of the 26th annual conference on Computer graphics and interactive techniques*, pages 121–128. ACM Press/Addison-Wesley Publishing Co., 1999. [7](#)
- [38] M. Strecke, A. Alperovich, and B. Goldluecke. Accurate depth and normal maps from occlusion-aware focal stack symmetry. In *Computer Vision and Pattern Recognition (CVPR), 2017 IEEE Conference on*, pages 2529–2537. IEEE, 2017. [2](#)
- [39] R. W. Sumner, J. Schmid, and M. Pauly. Embedded deformation for shape manipulation. In *ACM Transactions on Graphics (TOG)*, volume 26, page 80. ACM, 2007. [5](#)
- [40] T. T. Truscott, J. Belden, R. Ni, J. Pendlebury, and B. McEwen. Three-dimensional microscopic light field particle image velocimetry. *Experiments in Fluids*, 58(3):16, 2017. [2](#)
- [41] T. T. Truscott, J. Belden, J. R. Nielson, D. J. Daily, and S. L. Thomson. Determining 3d flow fields via multi-camera light field imaging. *Journal of visualized experiments: JoVE*, (73), 2013. [2](#)
- [42] B. Wieneke. Volume self-calibration for 3d particle image velocimetry. *Experiments in fluids*, 45(4):549–556, 2008. [2](#)
- [43] C. Willert and M. Gharib. Three-dimensional particle imaging with a single camera. *Experiments in Fluids*, 12(6):353–358, 1992. [2](#)
- [44] J. Xiong, Q. Fu, R. Idoughi, and W. Heidrich. Reconfigurable rainbow piv for 3d flow measurement. In *Computational Photography (ICCP), 2018 IEEE International Conference on*, pages 1–9. IEEE, 2018. [1, 2](#)
- [45] J. Xiong, R. Idoughi, A. A. Aguirre-Pablo, A. B. Aljedaani, X. Dun, Q. Fu, S. T. Thoroddsen, and W. Heidrich. Rainbow particle imaging velocimetry for dense 3d fluid velocity imaging. *ACM Transactions on Graphics (TOG)*, 36(4):36, 2017. [1, 2, 7](#)
- [46] T. Xue, M. Rubinstein, N. Wadhwa, A. Levin, F. Durand, and W. T. Freeman. Refraction wiggles for measuring fluid depth and velocity from video. In *European Conference on Computer Vision*, pages 767–782. Springer, 2014. [2](#)
- [47] J. Ye, Y. Ji, F. Li, and J. Yu. Angular domain reconstruction of dynamic 3d fluid surfaces. In *Computer Vision and Pattern Recognition (CVPR), 2012 IEEE Conference on*, pages 310–317. IEEE, 2012. [2](#)
- [48] J. Zhang, B. Tao, and J. Katz. Turbulent flow measurement in a square duct with hybrid holographic piv. *Experiments in Fluids*, 23(5):373–381, 1997. [2](#)